Table of Contents

List of Figures

Chapter 1

Glossary

EL Entrainment Layer

ML Mixed Layer

CBL Convective Boundary Layer

LES Large Eddy Simulation

FFT Fast Fourrier Transform

Ri Richardson Number , the bulk Richardson Number is $\frac{gh}{\overline{\theta}_{ML}}\frac{\Delta\theta}{w^{*2}}$, $\Delta\theta = \overline{\theta}(h_1) - \overline{\theta}(h_0)$

Chapter 2

Results

2.1 Description of Runs

All 10 member cases of the ensemble were carried out on a 3.2 x 4.8 Km horizontal domain ($\Delta x = \Delta y = 25m$, $nx = 128$, $ny = 192$). nx, ny were chosen based on the optimal distribution accross processor nodes. The vertical grid ($nz = 312$) was of higher resolution around the entrainment layer (EL) ($\Delta z = 5m$), and lower below and above it ($\Delta z = 10$ *to* $100m$). Grid size was chosen so that a full spectrum of turbulence would be resolved within the EL in line with the findings of Sullivan and Patton in [3]. The 7 runs vary depending on surface heat flux ($\overline{w'\theta'_s}$) and initial lapse rate (γ).

$\overline{w'\theta'_s}$ / γ	10 (K/Km)	5 (K/Km)	2.5 (K/Km)
150 (W/m2)	✓	✓[1]	
100 (W/m2)	✓	✓	
60 (W/m2)	✓	✓	✓

Table 2.1: Runs in terms of $\overline{w'\theta'_s}$ and initial lapse rate γ

[1]Incomplete run: EL exceded high resolution vertical grid after 7 hours

2.2 Relevant Definitions

In large eddy simulation (LES) studies, the CBL height is usually defined as either the point of minimum $\overline{w'\theta'}$ or maximum $\frac{\partial\overline{\theta}}{\partial z}$. A notable exception is the work of Brooks and Fowler in [1] where the authors favoured a statistically based definition using local tracer profiles. Similarly, they define the entrainment layer (EL) in terms of the statistics of local profiles, whereas elsewhere in the literature it is usually defined according to the zero crossings in the vertical $\overline{w'\theta'}$ profile.

Here, the CBL height and EL limits are defined based on the vertical $\frac{\partial\overline{\theta}}{\partial z}$ profile. Namely, the CBL height h is the point where $\frac{\partial\overline{\theta}}{\partial z}$ is maximum, the lower EL limit is the point at which $\frac{\partial\overline{\theta}}{\partial z}$ first increases significantly from zero i.e. exceeds a threshold value above the surface layer, and the upper EL limit h_1 is the point where $\frac{\partial\overline{\theta}}{\partial z}$ resumes γ. (Figure 2.1)

As Brooks and Fowler point out in [1], when using an average vertical tracer profile there is no universal critereon for a significant gradient. So a threshold value for the lower EL limit (h_0) was chosen such that it was positive, small i.e. an order of magnitude less than γ and the same for all runs. For the sake of rigor, the main corresponding result was calculated based on two additional threshold values in Section 2.6.3.

The temperature jump is defined here as the difference in $\overline{\theta}$ accross the EL. So, it is larger than those used by Federovich et al. in [2] to verify their zero order model and Sullivan et al. in [4] (Table 2.2).

CBL Height	θ Jump	Richardson Number
h	$\delta\theta = \overline{\theta}(h_1) - \overline{\theta}_{ML}$	$\mathrm{Ri}_\delta = \frac{\frac{g}{\theta}\delta\theta h}{w^{*2}}$
	$\Delta\theta = \overline{\theta}_{ML} - \overline{\theta}_0(h)$	Ri= $\frac{\frac{g}{\theta}\Delta\theta h}{w^{*2}}$

Table 2.2: Relevant Definitions used in this Study

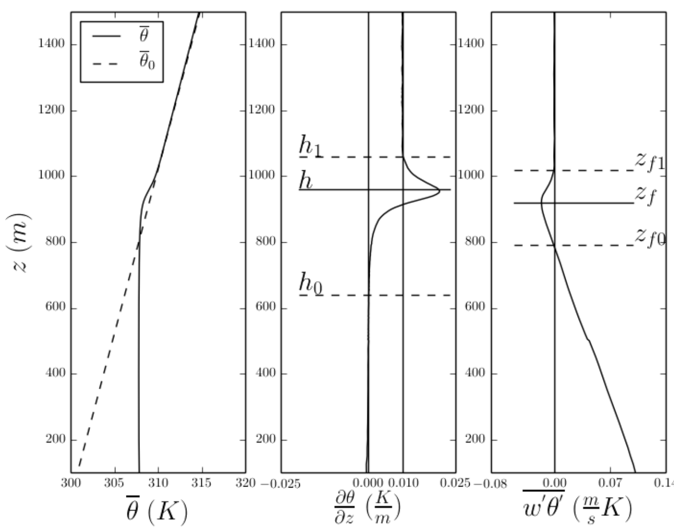

Figure 2.1: Height Definitions

2.3 Verifying the Model Output

2.3.1 Time till well-mixed

Time must be allowed to establish statistically steady turbulent flow. Sullivan et al. in [4] recommended 10 eddie turnover times based on the convective time scale $\tau = \frac{h}{w^*} = \frac{h}{\left(\frac{gh}{\overline{\theta}_{ML}}(\overline{w'\theta'_s})\right)^{\frac{1}{3}}}$, and Brooks and Fowler in [1] chose a simulated time of 2 hours. For all of the runs, at least 10 eddie turnover times were completed by 2 simulated hours (Figure 2.2). Although each run has a distinct convective velocity scale that increases with time ($w^*(time)$), dividing boundary layer height (h) by it to obtain τ results in a collapse from 7 to 3 curves, one for each γ.

A measureable well mixed layer (ML) and EL based on the horizontaly averaged, ensemble averaged potential temperature ($\overline{\theta}$) profile develops after 2 hours (Figure 2.3). After 2 or 3 hours the EL is fully contained within the vertical region of high resolution.

Averaged heat fluxes ($\overline{w'\theta'}$) (Figure 2.4) and root mean squared vertical velocity perturbations ($\sqrt{w'^2}$) (Figure 2.5) become self similar and are scaled well by the surface heat flux ($\overline{w'\theta'}_s$) and the convective velocity scale (w^*) respectively after 2 hours.

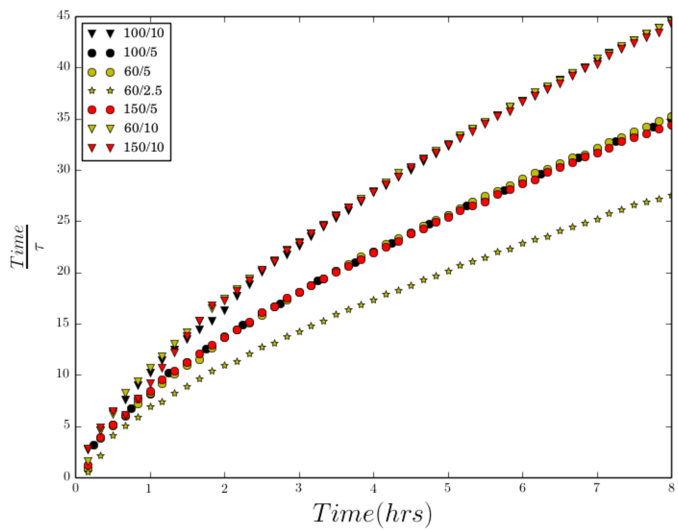

Figure 2.2: Plots of scaled time vs time for all runs. Scaled time is based on the convective time scale and can be thought of as the number of times an eddie has reached the top of the CBL.

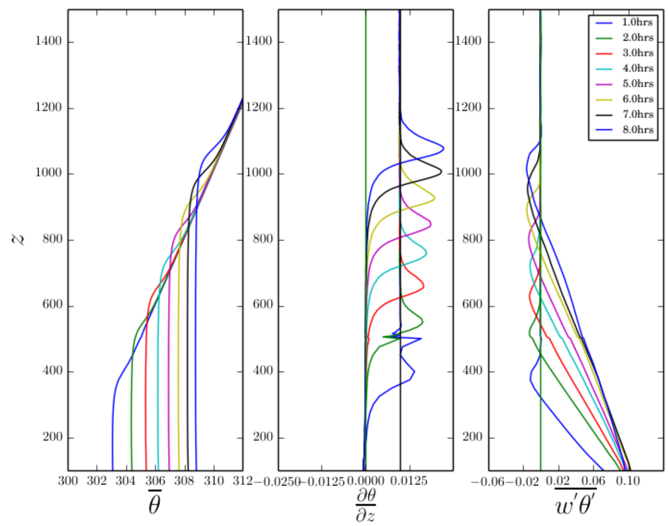

Figure 2.3: Vertical profiles of the ensemble and horizontally averaged potential temperature ($\overline{\theta}$), its vertical gradient ($\frac{\partial\overline{\theta}}{\partial z}$) and heat flux ($\overline{w'\theta'}$) for the 150/10 run

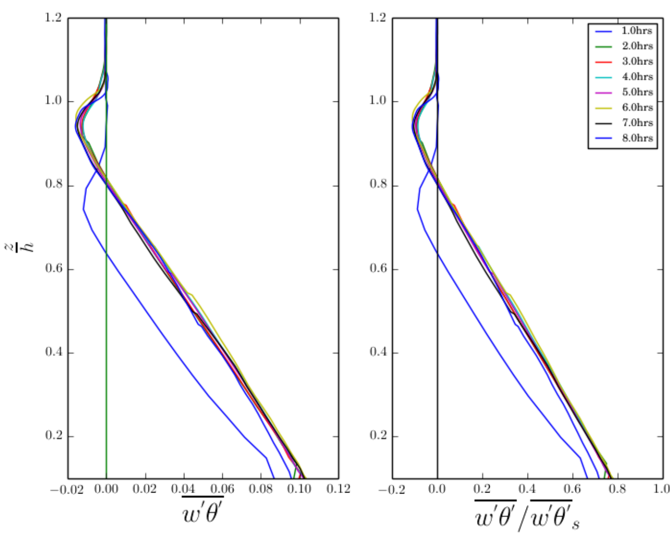

Figure 2.4: $\overline{w'\theta'}$ and scaled $\overline{w'\theta'}$ vs scaled height for the 150/10 run

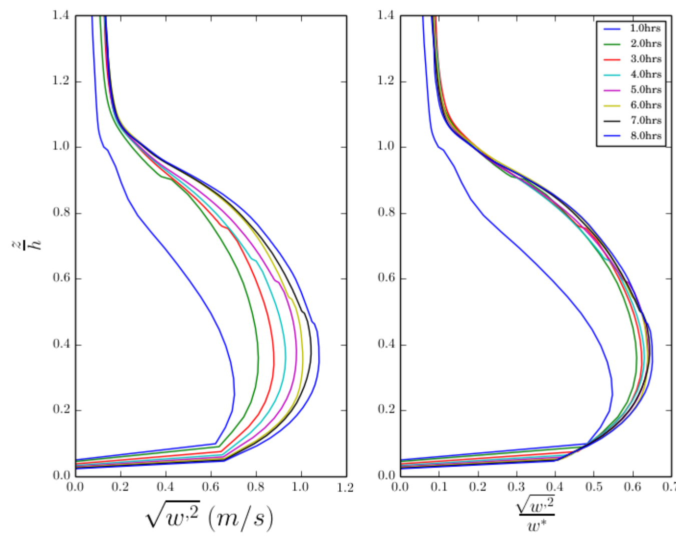

Figure 2.5: $\sqrt{w'^2}$ vs scaled height for the 150/10 run

2.3.2 FFT Energy Spectra

Two dimensional FFT power spectra taken of horizontal slices of $w^{'}$ (Figure 2.6) at three different levels (h_0, h and h_1) are collapsed to one dimension by integrating around a circle of wave-number radius k. Isotropy in all radial directions is assumed and $k = \sqrt{k_x^2 + k_y^2}$.

The resulting scalar density spectra show peaks in energy at the larger scales, cascading to the lower scales roughly according to a $\frac{-5}{3}$ slope, lower in the EL. At the top of the EL where turbulence is supressed by stability, the slope is steeper. The peak in energy occurs at smaller scales at the inversion (h) as compared to at the bottom of the EL (h_0), indicating a change in the size of the dominant turbulent structures further into the entrainment layer (EL).

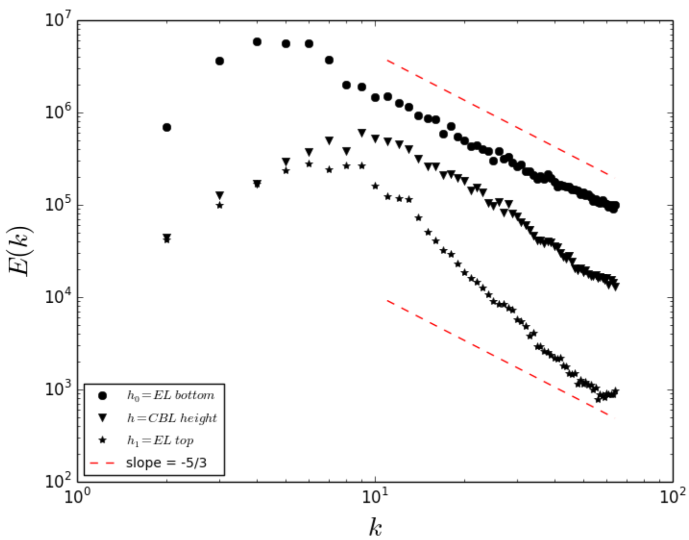

Figure 2.6: Scalar FFT energy vs wavenumber ($k = \sqrt{k_x^2 + k_y^2}$) for the 60/2.5 run at 2 hours. $E(k)$ is $E(k_x, k_y)$ integrated around circles of radius k. $E(k_x, k_y)$ is the total integrated energy over the 2D domain. k_x and k_y are number of waves per domain length.

2.3.3 Ensemble and horizontally averaged vertical Potential Temperature $\overline{\theta}$ and Heat Flux profiles $\overline{w'\theta'}$

The $\overline{\theta}$ profiles exhibit an ML above which $\frac{\partial\overline{\theta}}{\partial z} > 0$ and reaches a maximum value at h before resuming γ at h_1 (Figures 2.3 and 2.7). Convective boundary layer CBL growth is stimulated by $\overline{w'\theta'}_s$ and inhibited by γ.

The horizonally averaged, ensemble averaged heat flux ($\overline{w'\theta'}$) profiles decrease from the surface value ($\overline{w'\theta'_s}$) passing through zero to a minumum before increasing to zero (Figures 2.3 and 2.8). All minima are less in magnitude than the zero order approximation ($-.2 \times \overline{w'\theta'_s}$).

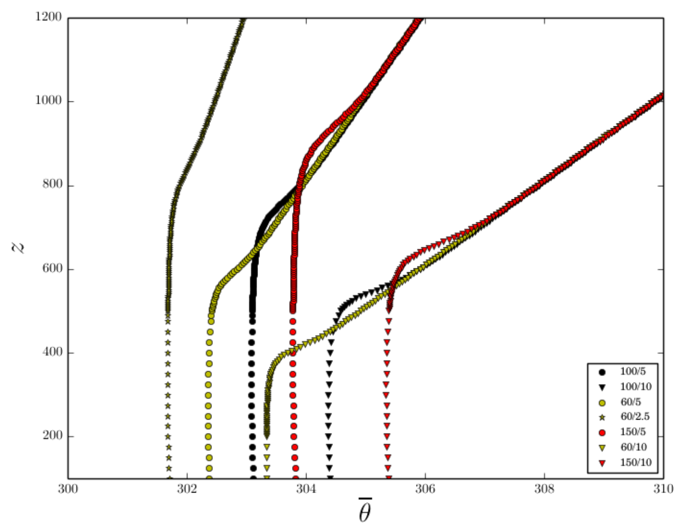

Figure 2.7: $\overline{\theta}$ profiles at 2 hours

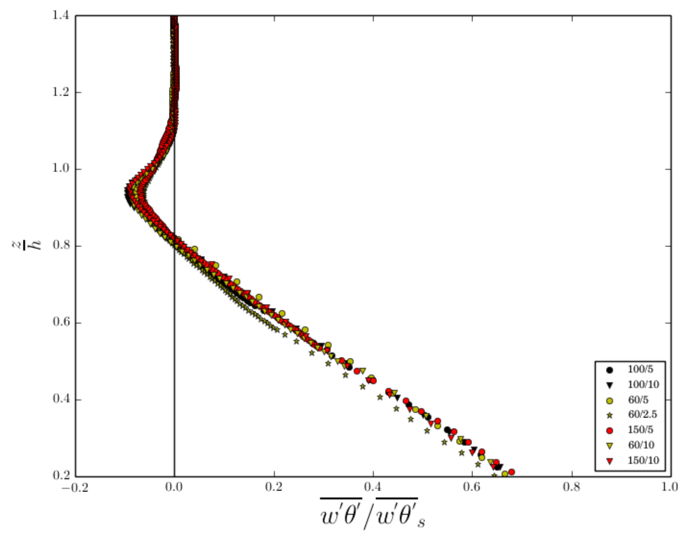

Figure 2.8: Scaled $\overline{w'\theta'}_s$ profiles at 2 hours

2.3.4 Visualization of Structures Within the Entrainment Layer

Horizontal slices, at the three entrainment layer (EL) levels, of the potential temperature and vertical velocity perturbations are plotted to see the turbulent structures. At the bottom of the EL (h_0) in the 150/10 run (Figure 2.9 (a) and (d)) coherent areas of positive and negative temperature perturbations correspond to areas of upward and downward moving air.

The individual plumes of relatively cool air are more evident at the inversion (h) and their locations correspond to areas of upward motion ((b) and (e)). Most of the upward moving cool areas are adjacent to and even encircled by smaller areas of downward moving warm air. At h_1 ((c) and (f)) peaks of cool air are associated with both up and down-welling.

In the 60/2.5 run (Figure 2.10) a similar progression is evident but the impinging, cool upward moving plumes are more defined. This is to be expected since stronger stability inhibits deformation of the inversion interface.

Figure 2.9: θ' (left) and w' (right) at 2 hours at h_0 (a,d), h (c,e) and h_1 (d,f)

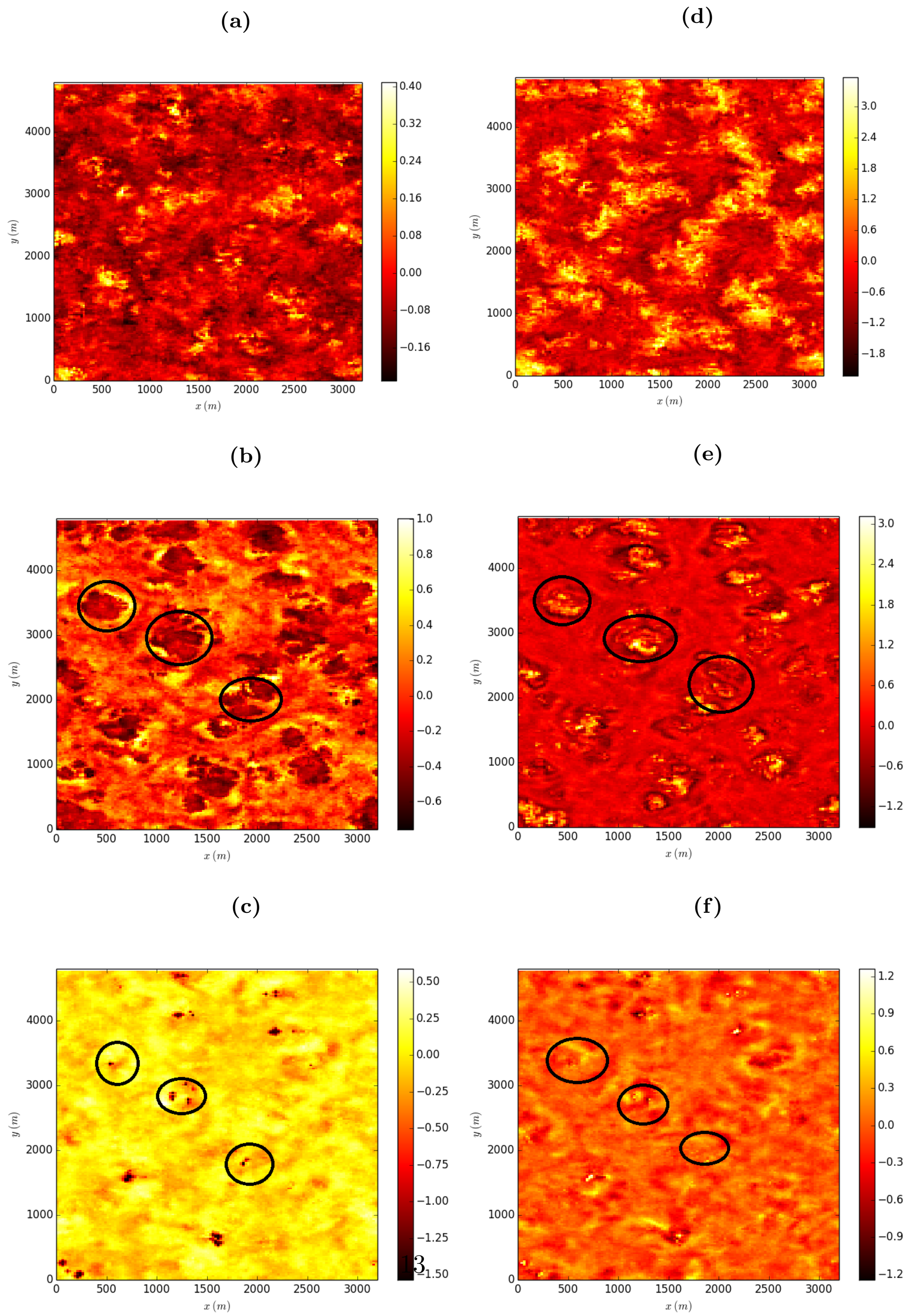

Figure 2.10: θ' (left) and w' (right) at 2 hours at h_0 (a,d), h(b,e) and h_1(c,f)

(a)

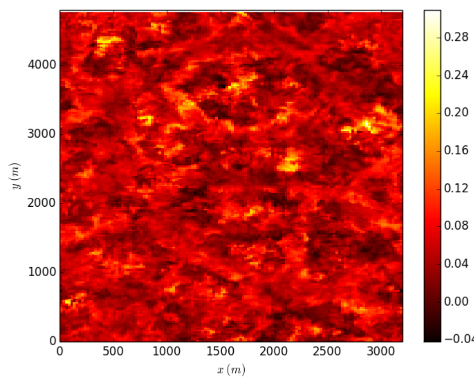

(d)

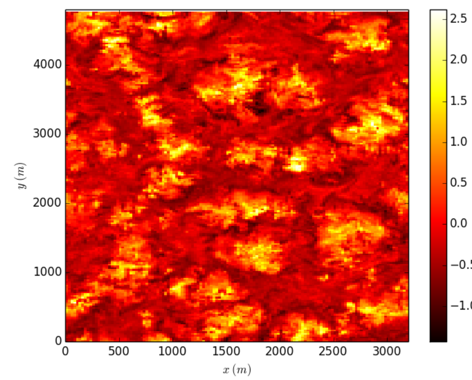

(b)

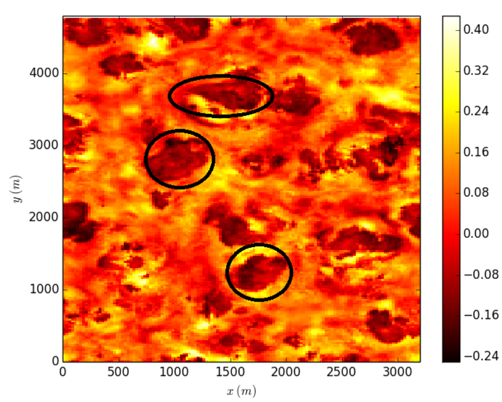

(e)

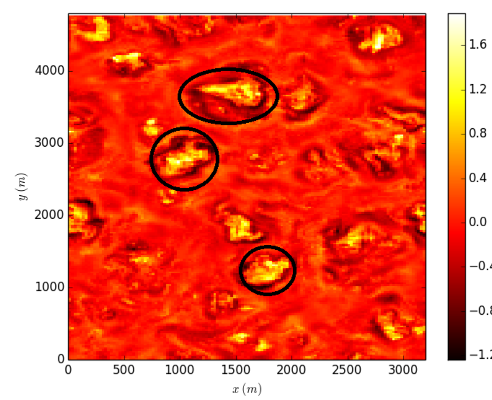

(c)

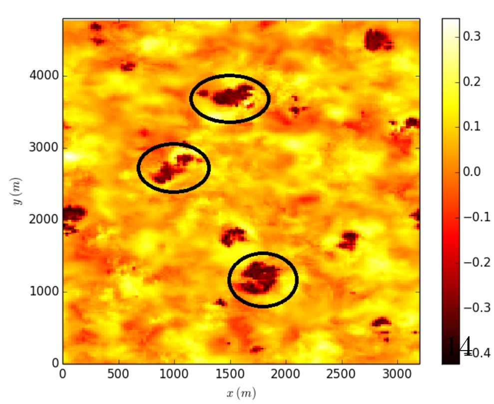

(f)

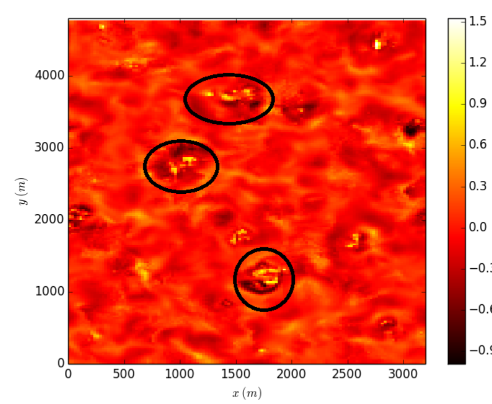

2.4 Local Mixed Layer Heights (h_0^l)

Local θ profiles (Figures 2.11 and 2.12) exhibit a distinct ML before resuming γ but not always a clearly defined EL. There are sharp changes in the profile well into the free atmosphere, due possibly to waves, which render the gradient method for determining h^l unusable. Instead a linear regression method is used, whereby three lines representing: the ML, the EL and the upper lapse rate (γ), are fit to the profile according to the minimum residual sum of squares (RSS). Determining local ML height (h_0^l) was more straight forward than the local height of maximum potential temperature gradient (h^l) for the reasons stated above.

Figure 2.11 shows two local θ profiles where h_0^l is relatively high. A sharp interface is evident indicating that this is within an active plume impinging on the stable layer. In Figure 2.12 where h_0^l is relatively low a less defined interface indicates a point now outside a rising plume. Contour plots (Figure 2.13) show regions of high h_0^l corresponding to regions of upward moving relatively cool air at h.

The distribution of h_0^l is related to the depth of the entrainment layer (EL). Spread increases with increasing $\overline{w'\theta'_s}$ and decreases with increasing γ (Figure 2.14). When scaled by h (Figure 2.15), the local ML height distribution has spread that narrows with increased γ and seems relatively uninfluenced by change in $\overline{w'\theta'}_s$. The upper limit seems to be constant at about $1.1(\times h)$, whereas the lower limit varies depending on γ. Runs with lower h and narrower Δh have relativiely larger spacing between bins and so higher numbers in each bin. The above supports the results outlined in Section 2.6.3.

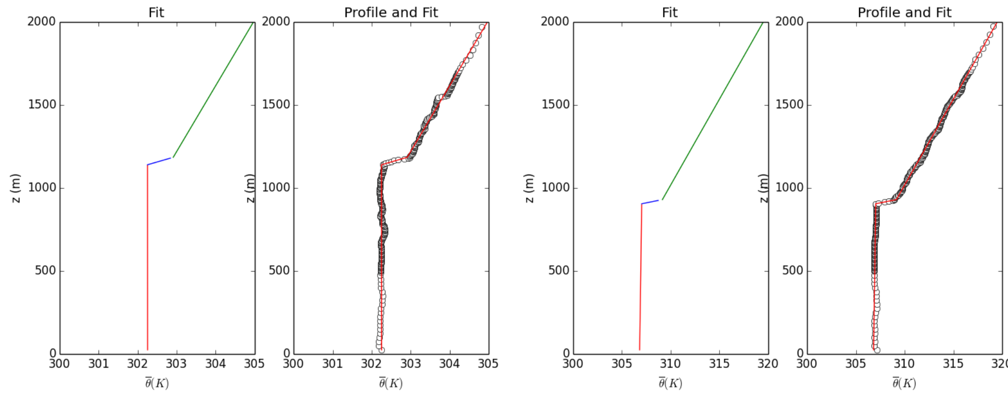

(a) **(b)**

Figure 2.11: Local vertical θ profiles with 3-line fit for the 60/2.5 (a) and 150/10 (b) runs at points where h_0^l is high.

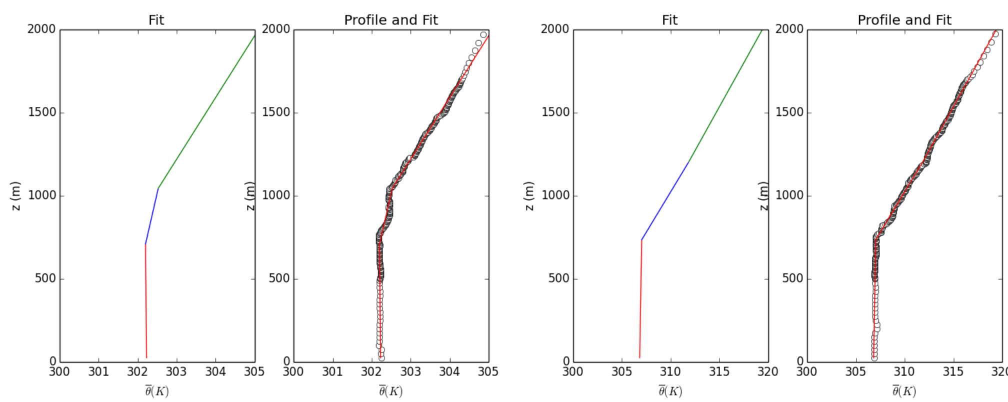

(a) **(b)**

Figure 2.12: Local vertical θ profiles with 3-line fit for the 60/2.5 (a) and 150/10 (b) runs at points where h_0^l is low.

Figure 2.13: θ' (a,d), w'(b,e) at h_1(c,f) and local ML height h_0^l at 2 hours for 60/2.5 (left) and 150/10 (right) runs

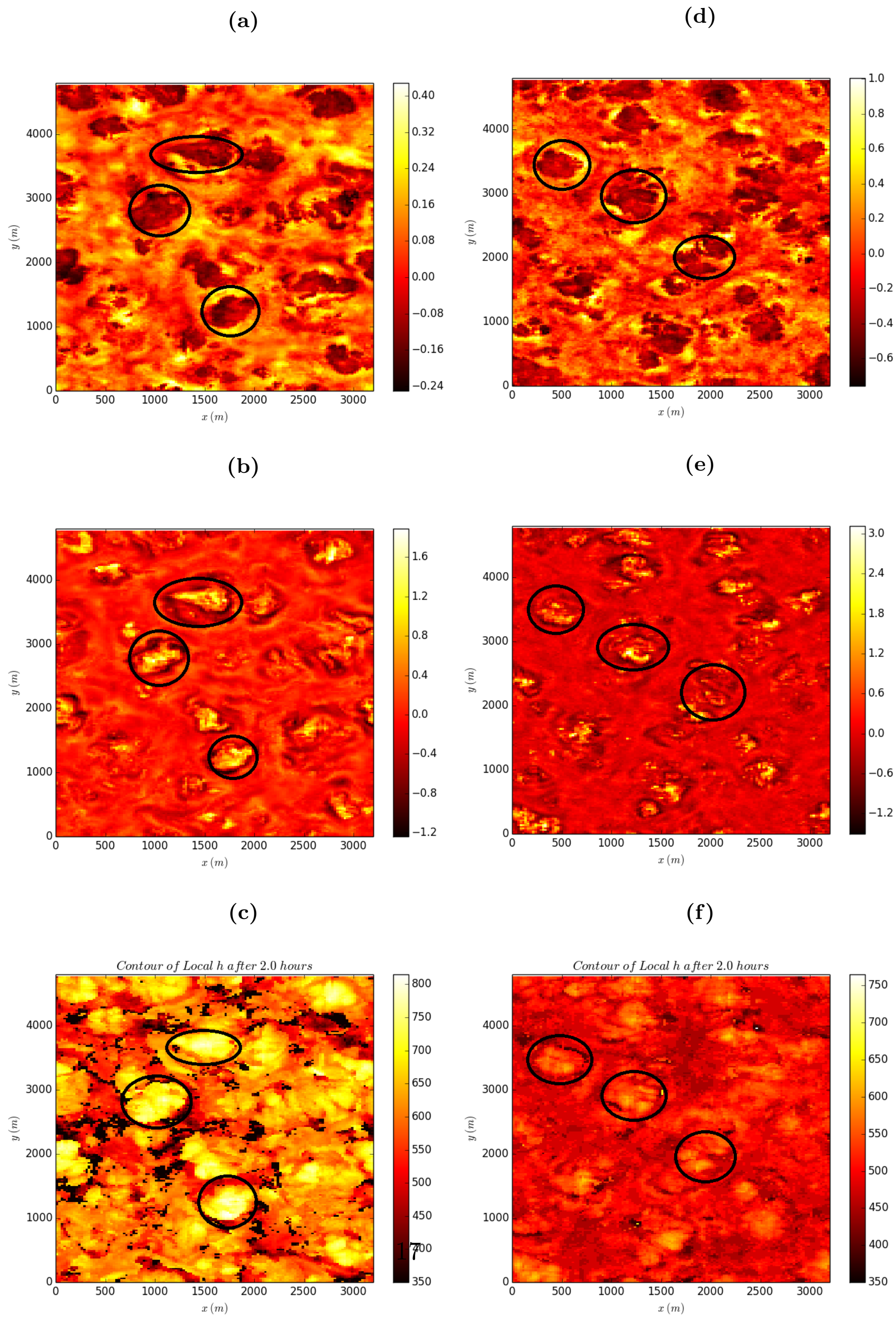

Figure 2.14: Histograms of h_0^l for $\overline{w'\theta'_s} = 150$ to $60(W/m^2)$ (a to c) and $\gamma = 10$ to $2.5(K/Km)$ (c to g) at 5 hours

(a)

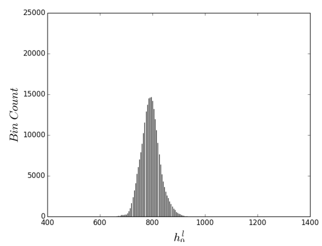

(d)

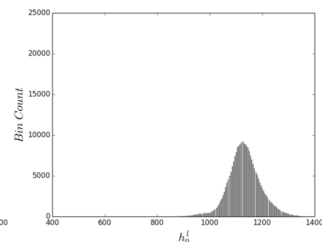

(b)

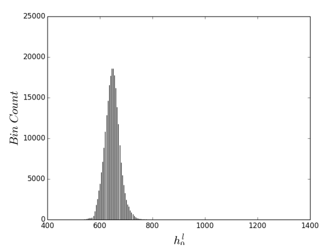

(e)

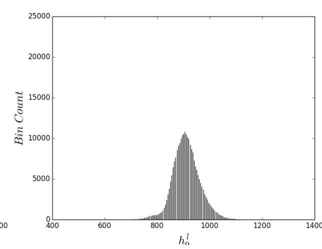

(c)

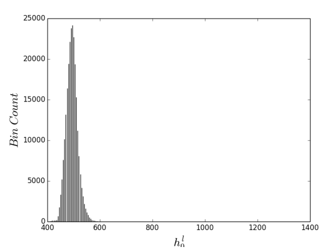

(f)

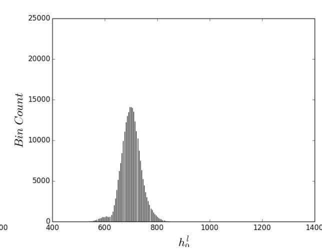

(g)

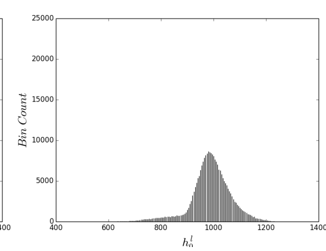

Figure 2.15: PDFs of $\frac{h_0^l}{h}$ for $\overline{w'\theta'_s} = 150$ to $60(W/m^2)$ (a to c) and $\gamma = 10$ to $2.5(K/Km)$ (c to g) at 5 hours

(a)

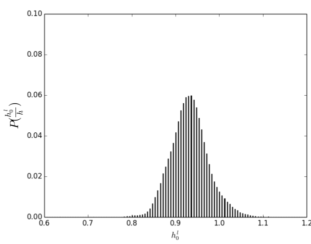

(d)

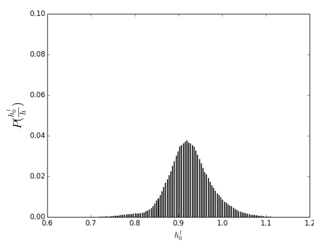

(b)

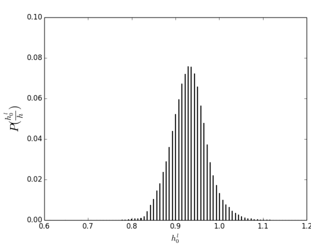

(e)

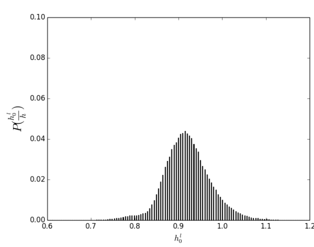

(c)

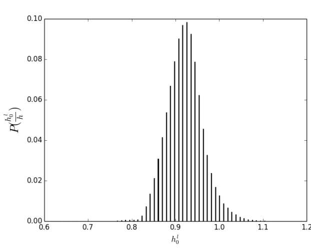

(f)

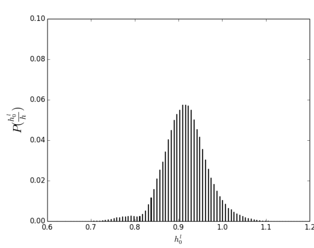

(g)

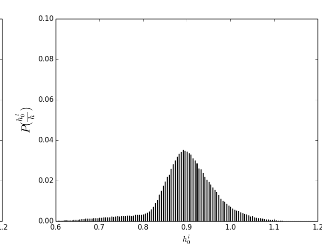

2.5 Flux Quadrants

As Sullivan et al. point out in [4] when broken out into four quadrants (Figure 2.16) the $\overline{w'\theta'}$ profiles have upper extrema above that of the total average profile (z_f). 2D histograms of the four quadrants are plotted at h_0, h and h_1 to see how the distributions are influenced by changes in $\overline{w'\theta'}$ and γ.

At h_0 (Figure **??**) fast updraughts are relatively warm. The spread in $w^{'}$ increases with increasing $\overline{w'\theta'}_s$ and decreases with increased γ. At h (Figure 2.16) the faster updraughts are now relatively cool and movement (both up and down) of warmer air from aloft becomes more prominent. The spread of $w^{'}$ and $\theta^{'}$ both increase with increasing $\overline{w'\theta'}$ whereas that of $\theta^{'}$ increases only slightly with increased stability. As expected stability inhibits both upward and downward $w^{'}$.

Although the quadrant of overall largest magnitude is that of upward moving cool air, Sullivan et al.'s assertion in [4] that in the EL the heat flux is effectively due to downward moving warm air because the other three quadrants cancel, is found to be approximately true. At the top of the EL (Figure 2.22) velocities are damped and the distributions approach symmetry apart from some slow, cool, impinging up- and down-draughts as in Figure 2.13.

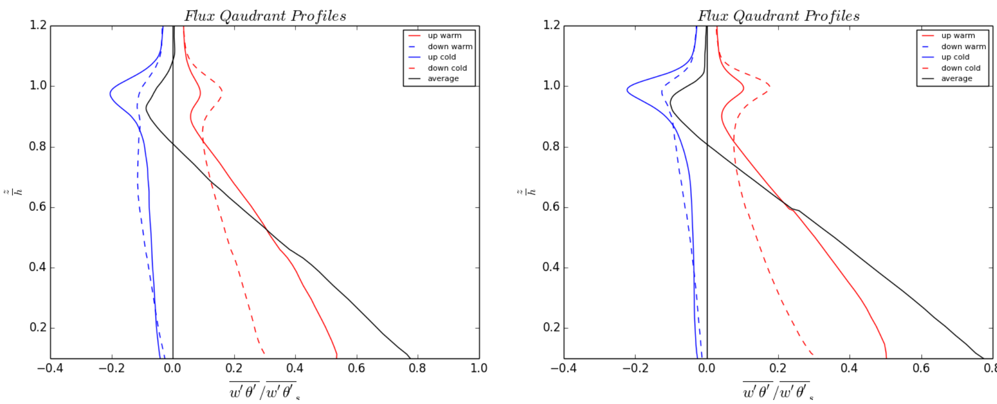

(a) **(b)**

Figure 2.16: Scaled $\overline{w'\theta'}$ quadrant profiles at 5 hours for the 60/2.5 (a) and 150/10 (b) run

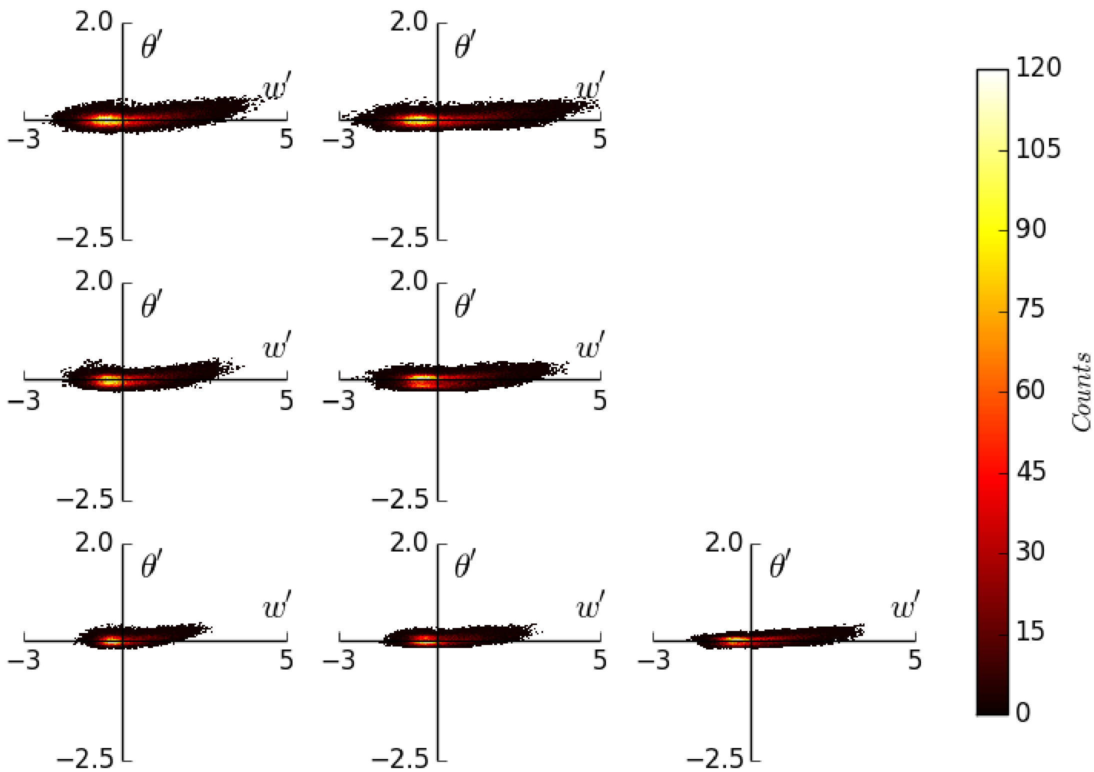

Figure 2.17: $\overline{w'\theta'}$ quadrants at h_0 for $w'\theta' = 150 - 60(W/m^2)$ (top-bottom) and $\gamma = 10 - 2.5(K/Km)$ (left-right) at 5 hours

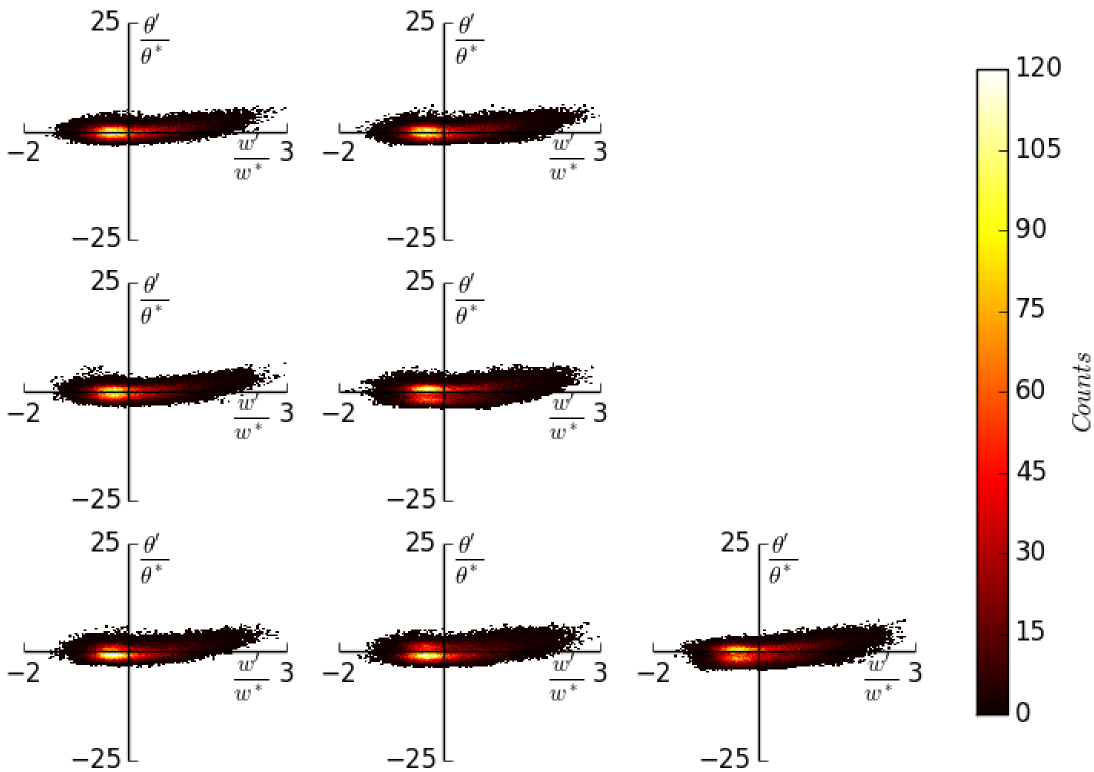

Figure 2.18: $\overline{w'\theta'}$ quadrants at h_0 for $w^{'}\theta^{'} = 150 - 60(W/m^2)$ (top-bottom) and $\gamma = 10 - 2.5(K/Km)$ (left-right) at 5 hours

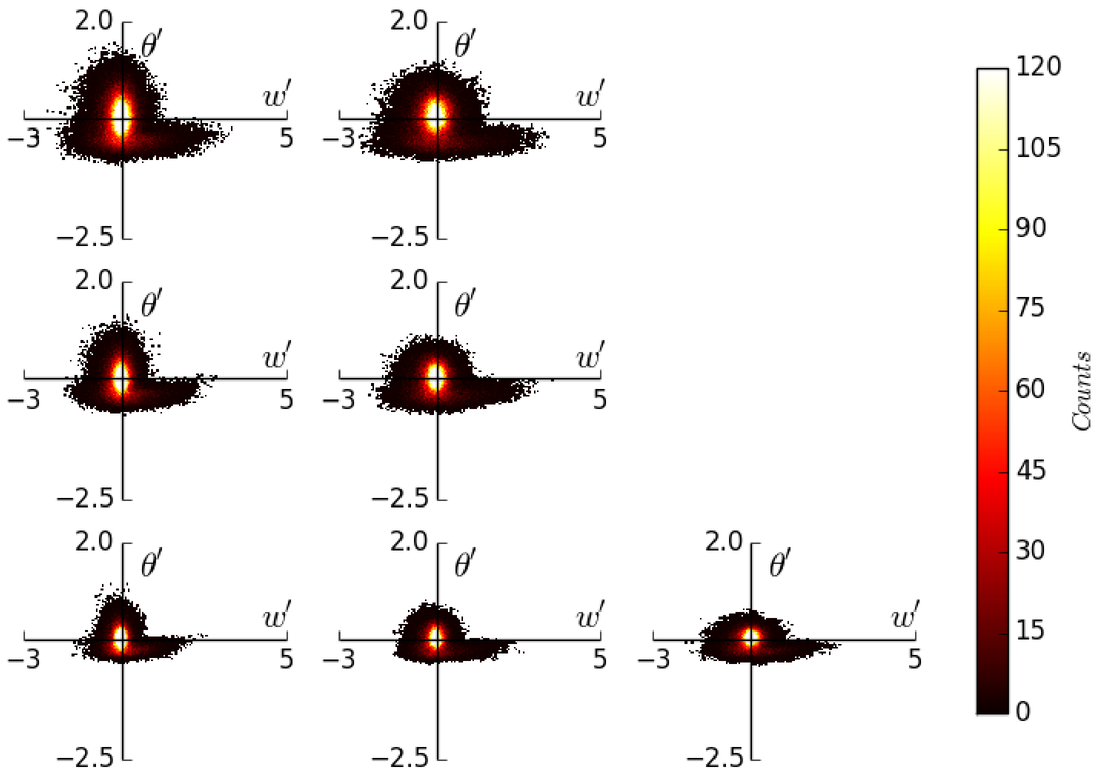

Figure 2.19: $\overline{w'\theta'}$ quadrants at h for $w^{'}\theta' = 150\ -\ 60(\mathrm{W}/m^2)$ (top - bottom) and $\gamma = 10\ -\ 2.5(\mathrm{K/Km})$ (left - right) at 5 hours

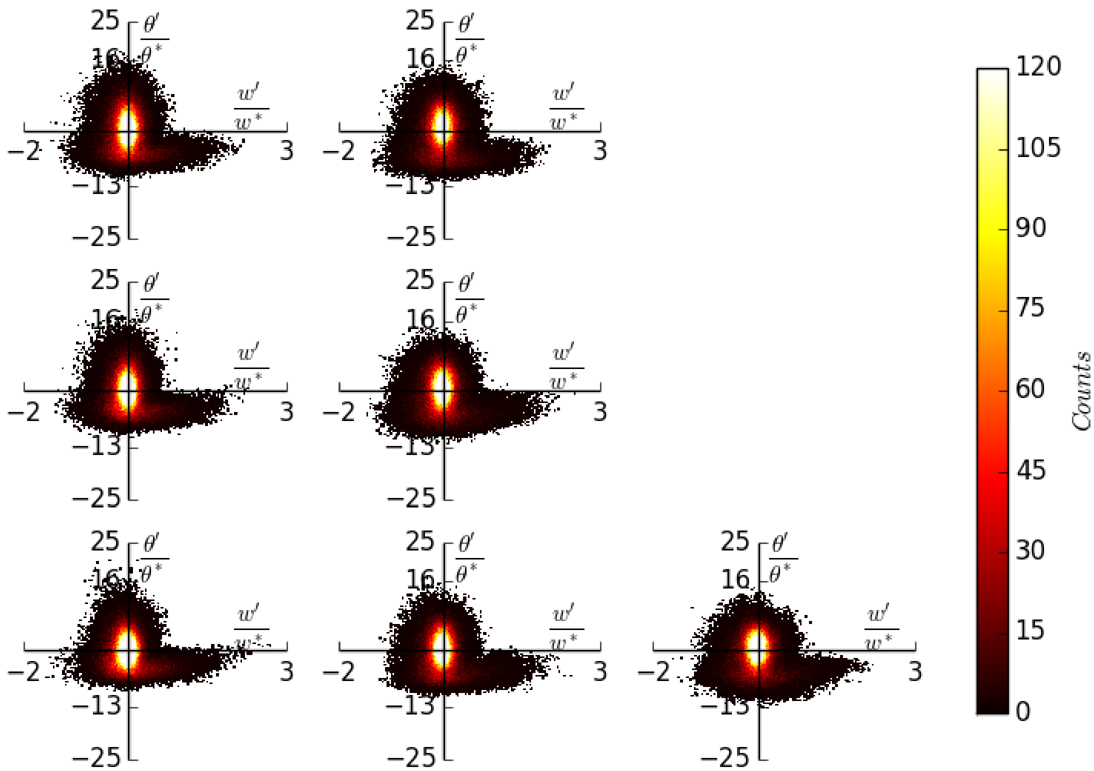

Figure 2.20: $\overline{w'\theta'}$ quadrants at h for $w'\theta' = 150 - 60(\mathrm{W}/m^2)$ (top - bottom) and $\gamma = 10 - 2.5(\mathrm{K/Km})$ (left - right) at 5 hours

Figure 2.21: $\overline{w'\theta'}$ quadrants at h_1 for $w'\theta' = 150$ *to* $60(\mathrm{W}/m^2)$ (top to bottom) and $\gamma = 10$ *to* $2.5(\mathrm{K/Km})$ (left to right) at 5 hours

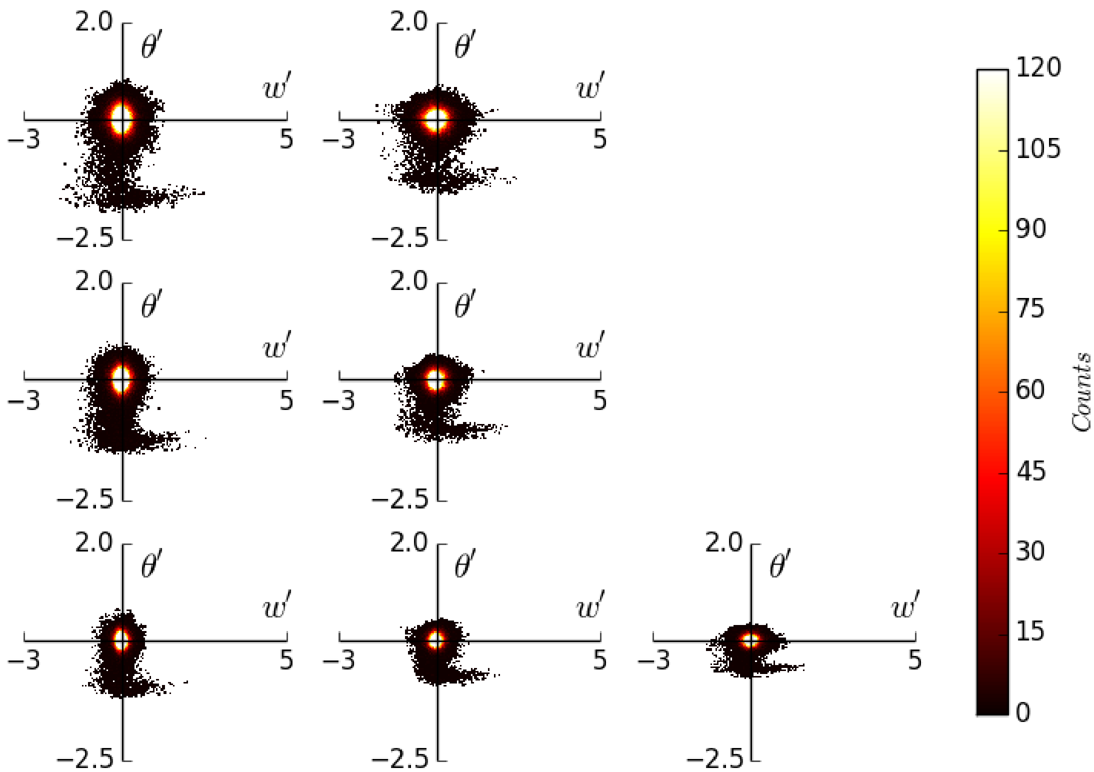

Figure 2.22: $\overline{w'\theta'}$ quadrants at h_1 for $w^{'}\theta^{'}$ = 150 *to* 60(W/m^2) (top to bottom) and $\gamma = 10$ *to* 2.5(K/Km) (left to right) at 5 hours

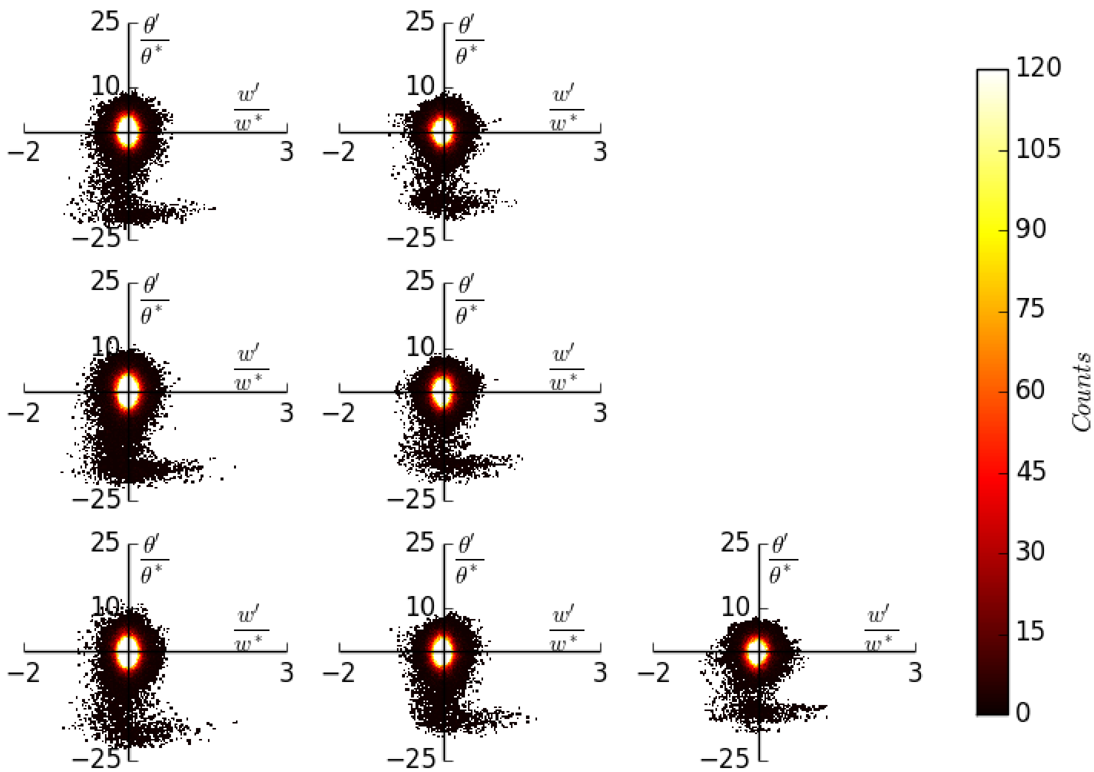

2.6 h and Δh based on Average Profiles

2.6.1 Reminder of Relevant Definitions

Here we define CBL height h as the point at which $\frac{\partial\bar{\theta}}{\partial z}$ is maximum and the EL limits: h_0 the point at which $\frac{\partial\bar{\theta}}{\partial z}$ first exceeds a threshold and h_1 the point at which $\frac{\partial\bar{\theta}}{\partial z}$ resumes γ. The temperature jump $\Delta\theta$ is the difference accross the EL.

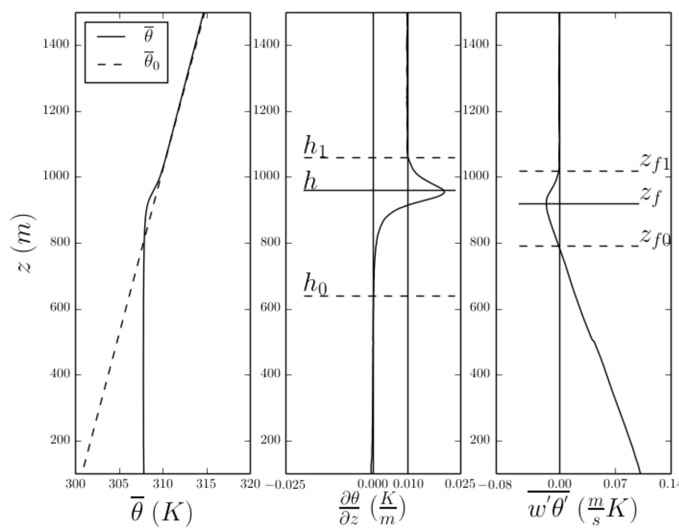

Figure 2.23: Height Definitions

Description	This Study	Sullivan et al. 1998	Fedorovich et al.[2]
CBL Height	h	h	z_f
Temperature Jump	$\Delta\theta = \overline{\theta}(h_1) - \overline{\theta}(h_0)$	$\Delta\theta = \overline{\theta}(z_{f1}) - \overline{\theta}(z_f)$	$\Delta b = b_0(z_f) - b(z_f)$ $\delta b = b(z_{f1})$ - $b(z_{f0})$
Convective Velocity Scale	$w_* = (hB_s)^{\frac{1}{3}}$, $B_s = \frac{g}{\theta_{ML}}\overline{w'\theta'}_s$	$w_* = (hB_s)^{\frac{1}{3}}$, $B_s = \frac{g}{\theta_{ML}}\overline{w'\theta'}_s$	$w_* = (z_f B_s)^{\frac{1}{3}}$
Richardson Number	$Ri = \frac{\Delta\theta h}{w^{*2}}$	$Ri = \frac{\Delta\theta h}{w^{*2}}$	$Ri_{\Delta b} = \frac{\Delta b z_f}{w^{*2}}$, $Ri_{\delta b} = \frac{\delta b_i z_f}{w^{*2}}$

Table 2.3: Comparison of relevant definitions with those from key publications

2.6.2 $\frac{w_e}{w^*}$ vs Ri^{-1}

Covective Boundary Layer (CBL) height (h) (Figure 2.24) grows rapidly initially with a steadily decreasing rate and relates to the square root of time (Figure2.25). It is found to be proportionate to the height of minimum flux (z_f) (Figure 2.26).

Inverse Richardson Number (Ri^{-1}) decreases with respect to time and clusters according to γ. (Figure 2.27). The entrainment rate ($w_e = \frac{dh}{dt}$) is determined from the slope of a second order polynomial fit to $h(time)$ (Figure 2.24). When scaled by (w^*) it is a roughly linear function of Ri^{-1} (Figure 2.28).

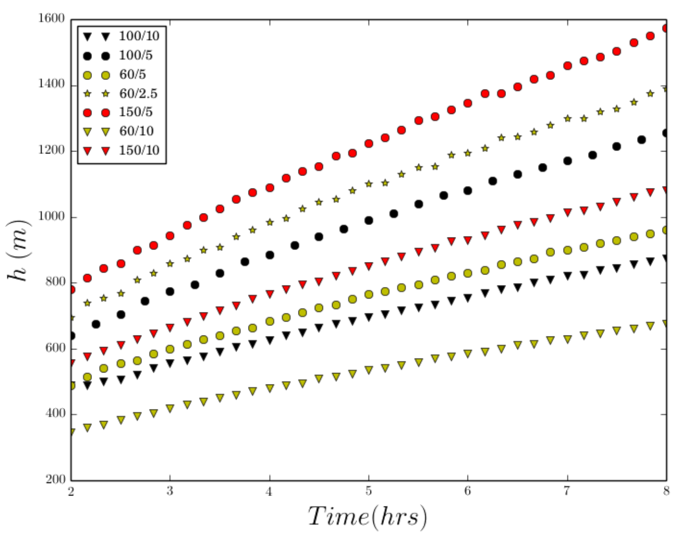

Figure 2.24: h vs time for all runs

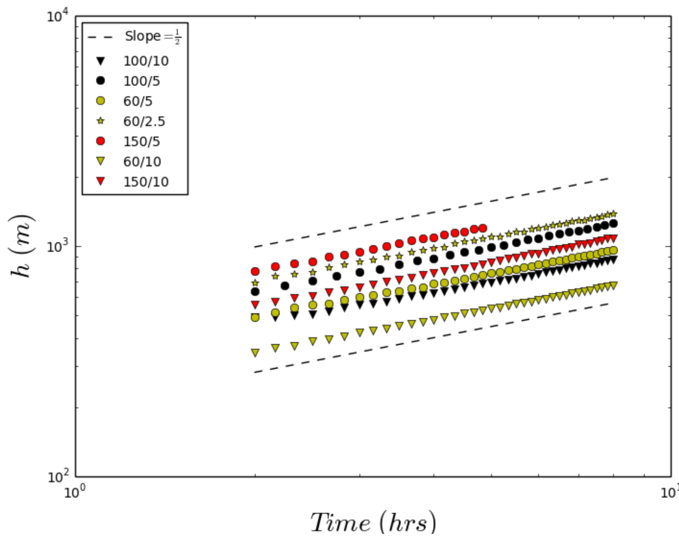

Figure 2.25: Log-Log plot of h vs time for all runs

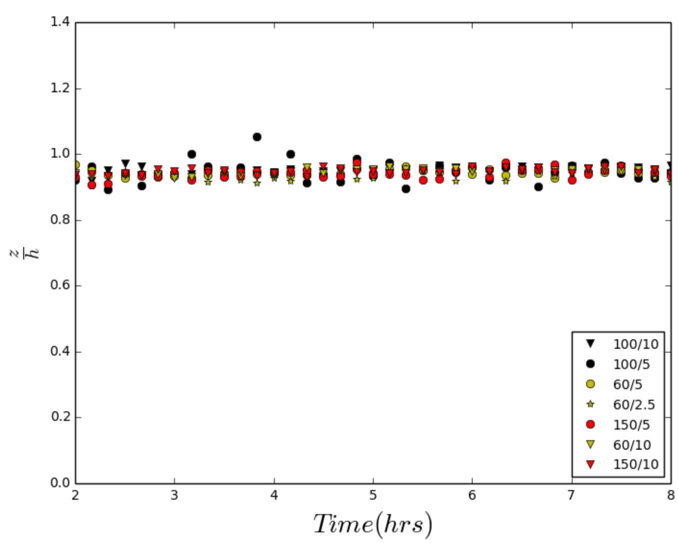

Figure 2.26: $\frac{z_f}{h}$ vs Time

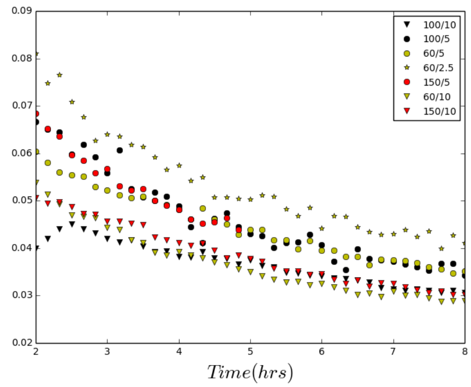

(a)

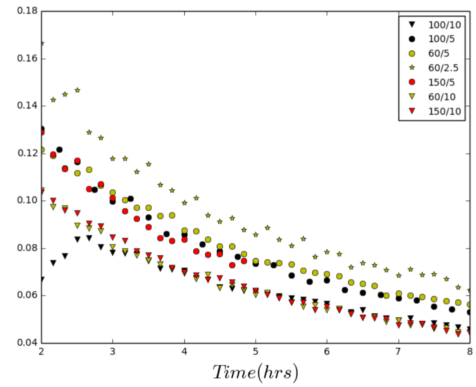

(b)

Figure 2.27: Inverse bulk Richardson Number vs time

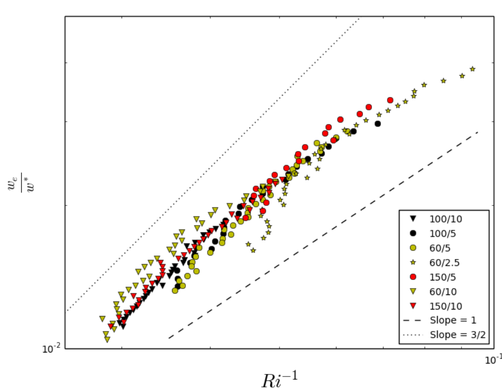

(a)

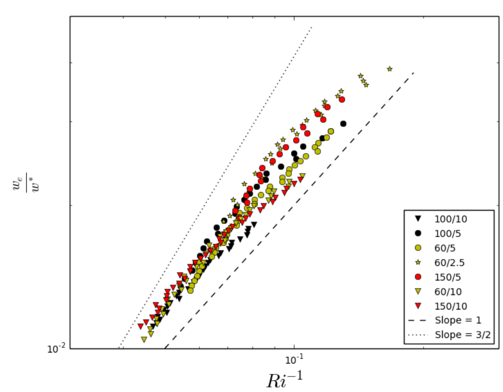

(b)

Figure 2.28: Scaled Entrainment rate vs inverse Richardson Number (Ri)

2.6.3 $\frac{\Delta h}{h}$ vs Ri^{-1}

The scaled upper EL limits ($\frac{h_1}{h}$) collapse well in Figure 2.29 to an initial value of approximately 1.15, decreasing to about 1.1. $\frac{h_0}{h}$s appear grouped according to γ and increase with respect to time. So overall the scaled EL appears to narrow with time. The scaled flux based EL (z_{f0} and z_{f1}) appears to remain constant with respect to time in Figure 2.30.

The lower entrainment layer limit h_0 is the point at which the vertical $\frac{\partial\overline{\theta}}{\partial z}$ exceeds a threshold (.0002) chosen such that it is positive, and at least an order of magnitude smaller than γ. Although the resulting scaled EL depth decreases with increasing Ri grouping according to γ is evident in Figure 2.32.

To explore how varying the threshold value affects the relationship between scaled EL depth and Richardson number (Ri), plots analogous to Figure 2.32 were produced at two additional thresholds. A higher threshold value (.0004) results in a higher h_0 (Figure 2.33) and so a narrower EL but a similar grouping according to γ (Figure2.34). A lower threshold value (.0001) results in a lower h_0 (Figure 2.35) but also similar grouping according to γ (Figure 2.36.

When the height definitions are based on the scaled vertical $\frac{\partial\overline{\theta}}{\partial z}$ i.e. $\frac{\partial\overline{\theta}}{\partial z}/\gamma$ profile, only h_0 changes and for clarity we call this EL depth Δh^* and the revised Richardson number Ri*. The curves now collapse and scaled EL depth is seen to decrease with increasing Ri* (Figures 2.37 to 2.39).

There is a slight collapsing effect on the scaled entrainment rate vs Ri relationship when the heights are defined based on the scaled vertical potential temperature gradient $\frac{\partial\overline{\theta}}{\partial z}/\gamma$ profile in Figure 2.40.

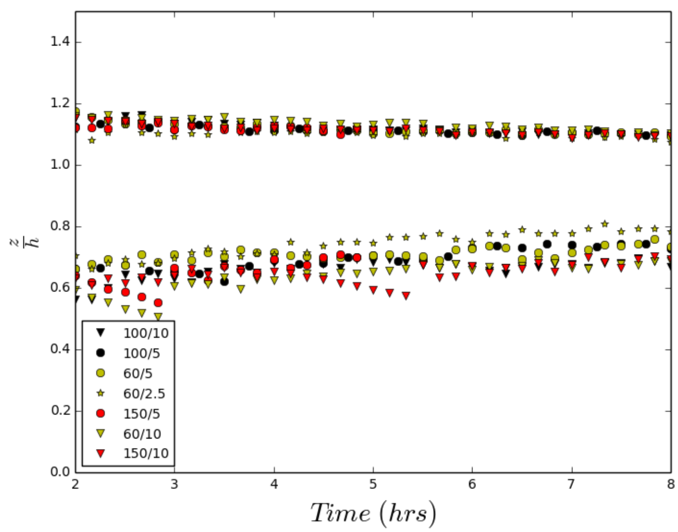

Figure 2.29: Scaled Entrainment Layer limits ($\frac{h_1}{h}$ and $\frac{h_0}{h}$) vs time

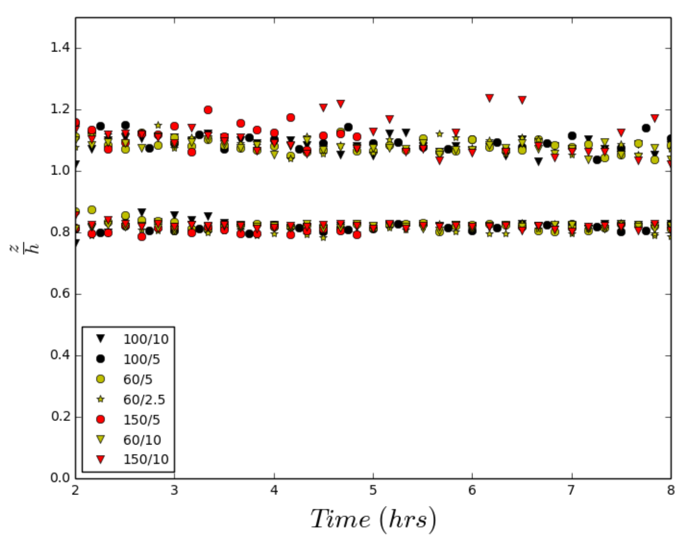

Figure 2.30: Scaled Entrainment Layer limits (z_{f1} and z_{f0}) vs time

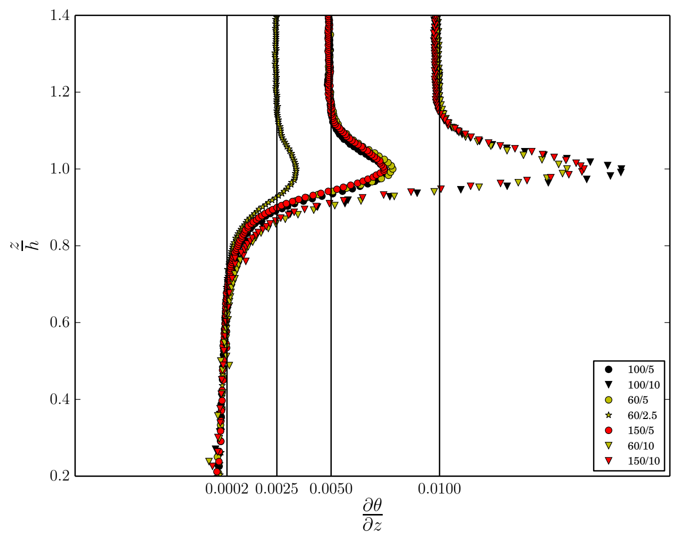

Figure 2.31: Vertical $\frac{\partial\overline{\theta}}{\partial z}$ profiles with threshold at .0002

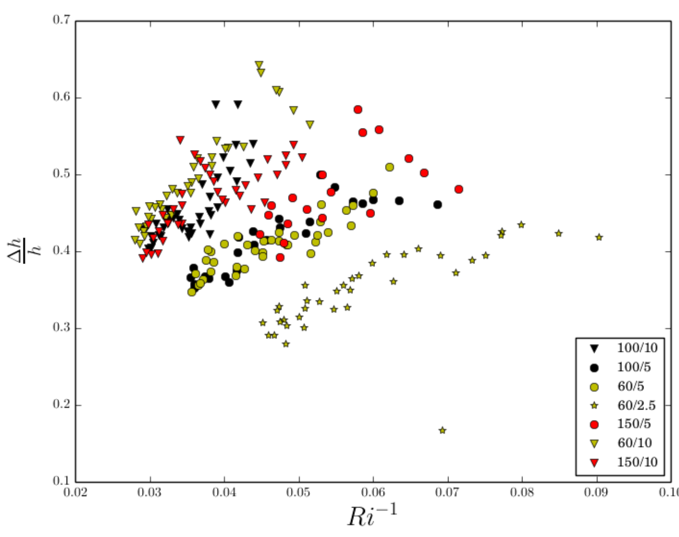

Figure 2.32: Scaled EL depth vs inverse bulk Richardson Number with threshold at .0002

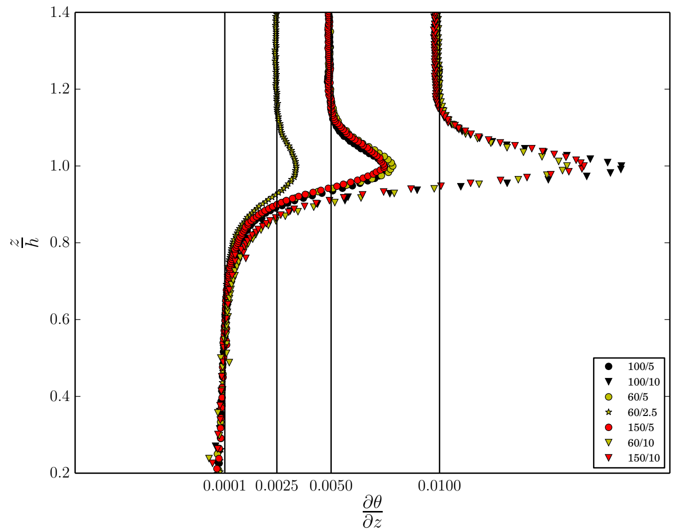

Figure 2.33: Vertical $\frac{\partial\overline{\theta}}{\partial z}$ profiles with threshold at .0004

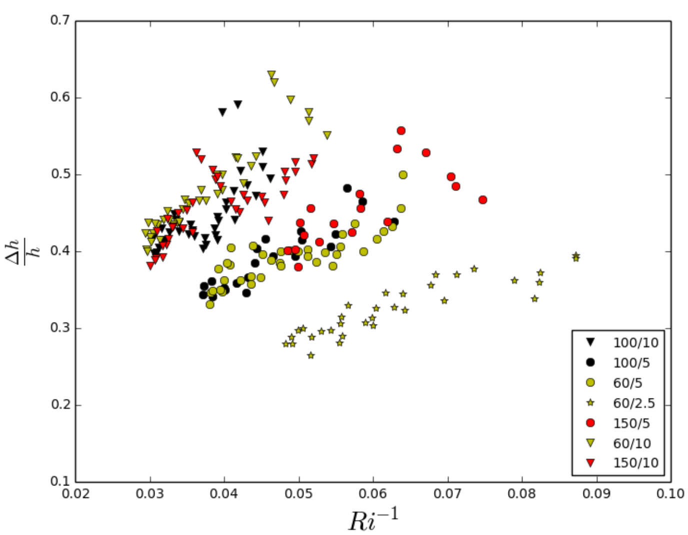

Figure 2.34: Scaled EL depth vs inverse Richardson Number with threshold at .0004

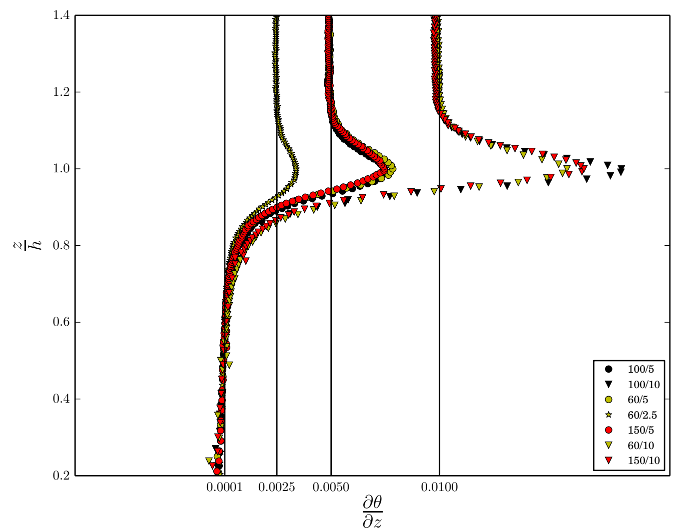

Figure 2.35: Vertical $\frac{\partial \overline{\theta}}{\partial z}$ profiles with threshold at .0001

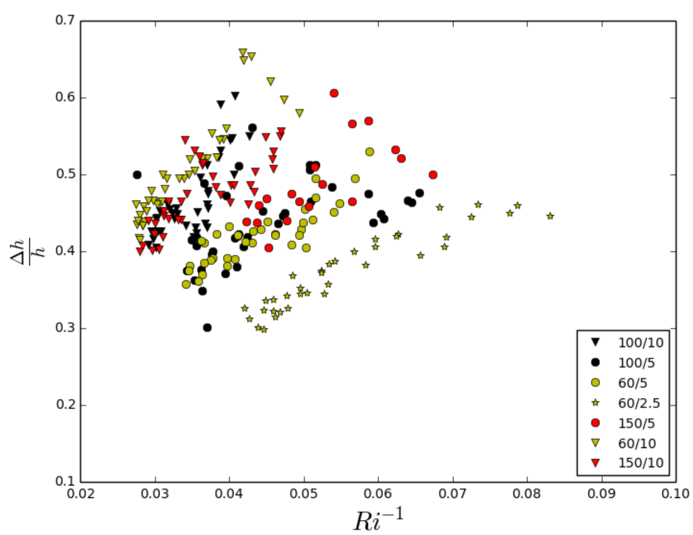

Figure 2.36: Scaled EL depth vs inverse bulk Richardson Number with threshold at .0001

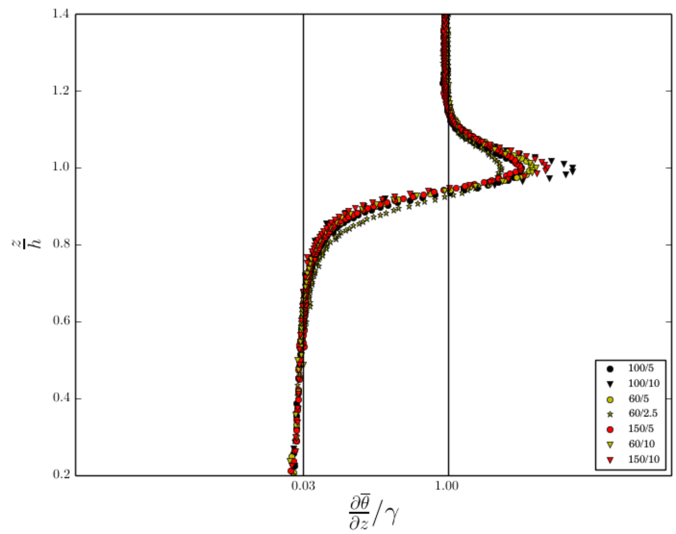

Figure 2.37: Scaled vertical $\frac{\partial\overline{\theta}}{\partial z}$ profiles with threshold at .03

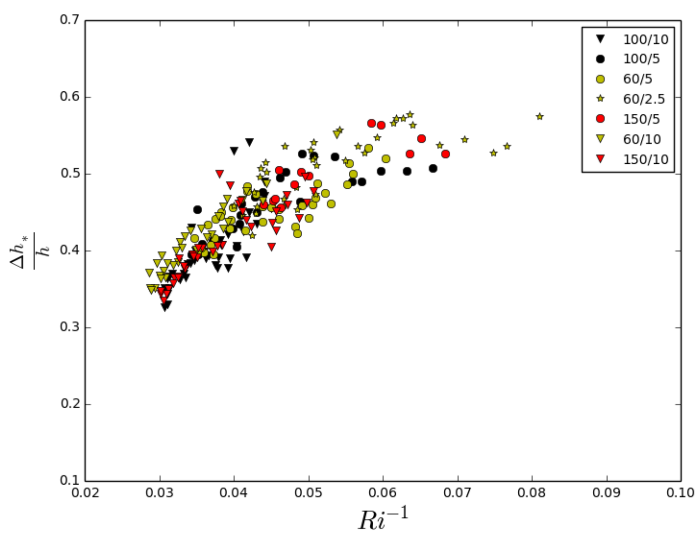

Figure 2.38: Revised height definitions based on scaled $\frac{\partial\overline{\theta}}{\partial z}$ profiles with threshold at .03

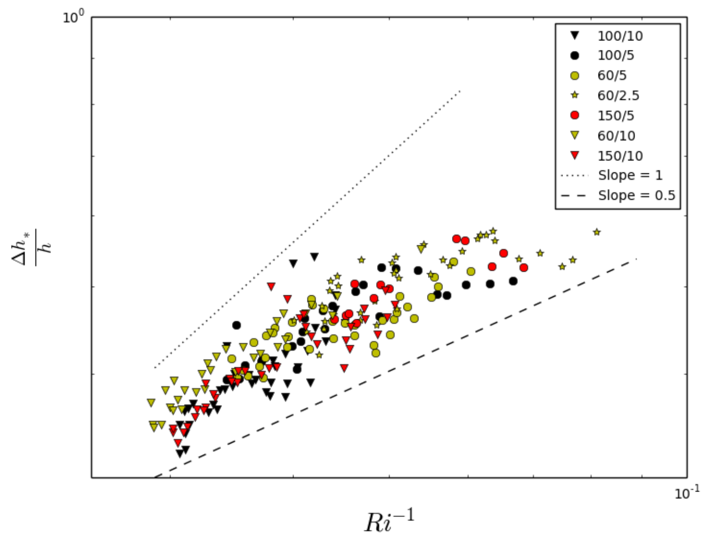

Figure 2.39: Scaled EL Depths vs inverse bulk Richardson number based on scaled $\frac{\partial \overline{\theta}}{\partial z}$ (a) and $\frac{\partial \overline{\theta}}{\partial z}$ (b)

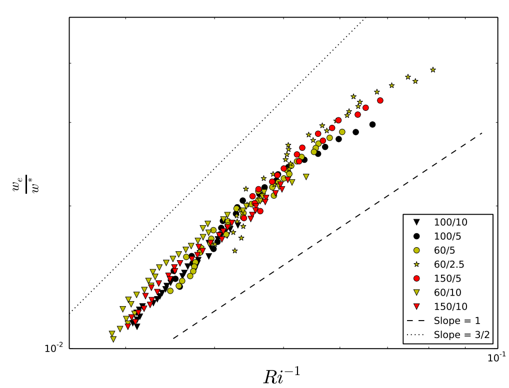

(a)

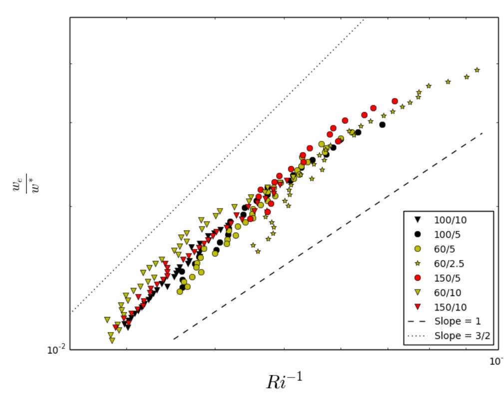

(b)

Figure 2.40: Scaled Entrainment Rate vs inverse bulk Richardson number based on scaled $\frac{\partial \overline{\theta}}{\partial z}$ (a) and $\frac{\partial \overline{\theta}}{\partial z}$ (b)

Bibliography

[1] I. M. Brooks and A. M. Fowler. An evaluation of boundary-layer depth, inversion and entrainment parameters by large-eddy simulation. *Bundary-Layer Meteorology*, 142:245–263, 2012. → pages 2, 4

[2] E. Federovich, R. Conzemus, and D. Mironov. Convective entrainmnent into a shear-free, linearly stratifies atmosphere: Bulk models reevaluated through large eddie simulation. *Journal of the Atmospheric Sciences*, 61:281 – 295, 2004. → pages 2, 29

[3] P. P. Sullivan and E. G. Patton. The effect of mesh resolution on convective boundary layer statistics and structures generated by large eddie simulation. *Journal of the Atmospheric Sciences*, 58:2395–2415, 2011. doi:10.1175/JAS-D-10-05010.1. → pages 1

[4] P. P. Sullivan, C.-H. Moeng, B. Stevens, D. H. Lenschow, and S. D. Mayor. Structure of the entrainment zone capping the convective atmospheric boundary layer. *Journal of the Atmospheric Sciences*, 55: 3042–3063, 1998. doi:10.1007/s10546-011-9668-3. → pages 2, 4, 20, 29